RSC Advances

PAPER

View Article Online
View Journal | View Issue

Check for updates

Cite this: *RSC Adv.*, 2024, **14**, 15604

Enhanced photocatalytic activity of porous TiO_2 containing C/P/K derived from grapefruit peel†

Ruixiang Wu, [ab] Wenhua Liu,*[a] Renao Bai, [b] Xiufang Tian,[b] Weikai Lin,[b] Lejian Li[b] and Qianwei Ke[b]

Grapefruit peel possesses a porous structure and a significant specific surface area. In this study, we introduce an innovative and eco-friendly approach for synthesizing porous TiO_2. This was accomplished by employing grapefruit peel as a bio-template and tetrabutyl titanate as the precursor, utilizing a two-step rotary impregnation-calcination process. The TiO_2 faithfully reproduced the structural characteristics of the grapefruit peel across different scales, simultaneously incorporating C, P, K elements from the original grapefruit peel into the final samples. The fabricated samples were analyzed using XRD, XPS, SEM, TEM, BET, and UV-vis DRS. The results showed that the TiO_2 displays an anatase phase, and possesses a high specific surface area. The investigation of photocatalytic performance demonstrated that the CPK-TiO_2-10 sample exhibited outstanding photocatalytic activity against Rhodamine B (RhB) solution, achieving complete degradation within 60 minutes. Additionally, the total organic carbon (TOC) removal rate reached 91.34% after 60 minutes of irradiation. The sample maintained a high degradation efficiency, even after five recycling cycles. This exceptional performance can be attributed to its porous structure, enriched with pores and a larger surface area, as well as the beneficial effects of doping with C, P, K elements in TiO_2.

Received 22nd March 2024
Accepted 23rd April 2024

DOI: 10.1039/d4ra02180k

rsc.li/rsc-advances

Open Access Article. Published on 14 May 2024. Downloaded on 1/20/2026 11:48:06 AM.
This article is licensed under a Creative Commons Attribution-NonCommercial 3.0 Unported Licence.

1 Introduction

Water pollution poses a significant threat to both the environment and human health.[1] Among the various contributors to water pollution, dyes have emerged as a major concern.[2] Global reports indicate an annual production of more than 700 000 tons of dyes, with more than one-tenth of this quantity being discharged into the environment untreated during production and use.[3,4] Due to their inherent resistance to natural degradation, dyes present a formidable challenge, necessitating the development of effective methods and technologies for the purification and treatment of contaminated dye wastewater. In response to this environmental challenge, photo-catalytic degradation technology has gained prominence as a rapid and efficient means of removing pollutants from wastewater. Over recent years, this technology has found widespread application in the treatment of dye wastewater.[5,6]

As the most promising photocatalyst, TiO_2 has been widely used in the field of environmental governance.[7–10] With the capability to photocatalytically degrade most organic pollutants, TiO_2 demonstrates several advantages, including better stability, environmental friendliness devoid of toxic side effects, and lower cost.[11–13] Consequently, it has been recognized as the most representative material for photocatalytic treatment of organic pollutants in water. However, despite its prominence, TiO_2 photocatalysts face several challenges in practical application, such as low quantum efficiency, low visible light utilization, and harsh preparation conditions.[11–13] These problems severely impede the practical applicability of TiO_2. Studies have shown that photocatalytic performance is profoundly influenced by the structure and morphology of the catalyst. The traditional preparation methods make it hard to meet the demand for directional and precise control of the structure and performance of the materials. Hence, there exists a formidable challenge in the field, the preparation of TiO_2 photocatalytic materials with controllable morphology and structure, coupled with exceptional performance, using a straightforward and efficient method.

Originating from the philosophical concept of "learning from nature", the preparation of novel functional materials with multilevel fine and complex structures using natural biomaterials as templates is a relatively cutting-edge research field, which has attracted the attention of domestic and foreign researchers.[14,15] Some researchers utilized various natural materials as bio-templates to improve the morphology and structure of TiO_2, while simultaneously incorporating elements from biomass into TiO_2, achieving synergistic enhancement of

[a]*Guangdong Provincial Laboratory of Marine Biotechnology, Institute of Marine Sciences, Shantou University, Guangdong 515063, P. R. China. E-mail: whliu@stu.edu.cn*

[b]*College of Construction and Ecology, Shantou Polytechnic, Guangdong 515078, P. R. China*

† Electronic supplementary information (ESI) available. See DOI: https://doi.org/10.1039/d4ra02180k

© 2024 The Author(s). Published by the Royal Society of Chemistry

Open Access Article. Published on 14 May 2024. Downloaded on 1/20/2026 11:48:06 AM.
This article is licensed under a Creative Commons Attribution-NonCommercial 3.0 Unported Licence.

TiO_2 photocatalytic activity. Li *et al.*[16] employed green leaves, resulting in N-doped leaf-shaped TiO_2, with morph-TiO_2 derived from different leaves showing a significant increase (103–258%) in absorbance intensity within the visible light range. Chen *et al.*[17] utilized rose petals as bio-templates, producing doped N bio-morphic TiO_2 films exhibiting heightened photocatalytic activity against methylene blue degradation under sunlight. Turkten *et al.*[18] utilized rice husk (RH) as a bio-template to fabricate TiO_2 hierarchical microstructure photocatalysts (TiO_2-HMP) doped with C, N, S, and Si elements. TiO_2-HMP, compared to the control TiO_2-NP, demonstrated a reduced band gap of 0.46 eV and an augmented surface area of approximately 10%. When exposed to UV light, TiO_2-HMP showed a photocatalytic activity enhancement (≥10%) compared to TiO_2-NP, likely attributed to the *in situ* self-codoping of RH by the presence of multiple dopant ions (C, N, S, and Si).

Grapefruit peel, possesses a porous structure and a significant specific surface area, often considered agricultural waste, is typically discarded without any effective application, leading to the unnecessary loss of biomass resources and indirectly exacerbating environmental pollution.[19] Comprising various substances such as cellulose, hemicellulose, lignin, glucose, and pectin.[20] Consequently, its surface is enriched with hydroxyl, carboxyl, and other functional groups,[21] which can attract cations through electrostatic forces and chelation. Grapefruit peel, as a readily available and environmentally benign resource, holds significant promise for the bio-inspired synthesis of inorganic materials. Moreover, various functional materials have been prepared by using grapefruit peel as a biological template. Zhu *et al.*[22] deposited hexadecyl trimethyl ammonium bromide/TiO_2 composites using grapefruit peel as a template. After calcination-acid treatment to remove the grapefruit peel, TiO_2 foam was obtained, which is used as an adsorbent to enrich peptides. Zhao *et al.*[23] utilized grapefruit peel as a template to prepare $LaFeO_3$ perovskite with a large number of micro–nano pore structures, which showed a high conversion efficiency of 94% for nitric oxide. Zhang *et al.*[24] utilized grapefruit peel to prepare biochar, and then grew TiO_2 on the biochar to prepare grapefruit peel TiO_2/biochar composite material. The composite material exhibited a photocatalytic degradation of tetracycline under simulated sunlight, with an apparent rate constant of 0.021 min^{-1}.

In contrast to prior investigations, we used grapefruit peel as a bio-template to modulate the morphology and structure of TiO_2, while allowing for the natural integration of bio-elements from grapefruit peel into TiO_2. By improving the structure and elemental composition of TiO_2, we achieve synergistic enhancements in the photocatalytic activity of the resultant TiO_2. In this study, a simple yet effective method was applied, utilizing grapefruit peel as both a reactive substrate and a template; tetrabutyl titanate was used as the precursor to synthesize porous TiO_2 containing C/P/K. The synthesis proceeded *via* a two-step process, including rotary impregnation and calcination. The produced samples underwent extensive characterization. Furthermore, the photocatalytic activity of these samples was assessed by the degradation of Rhodamine B (RhB) under UV light irradiation.

2 Materials and methods

2.1 Materials

Grapefruit peels were purchased from Shantou Agricultural and Trade Market, Shantou, China. The following chemicals were utilized: tetrabutyl titanate (500 mL, AR) acquired from Shanghai Macklin Company Limited; RhB (100 g, AR) purchased from Shanghai Macklin Biochemical Technology Co., Ltd; as well as sodium hydroxide (500 g, AR), sodium chloride (500 g, AR), anhydrous ethanol (500 mL, AR), acetic acid (500 mL, AR), and nitric acid (500 mL, AR) both procured from Sinopharm Chemical Reagent Co., Ltd.

2.2 Preparation of CPK-TiO_2 photocatalysts

The grapefruit peel collected for this study underwent a meticulous preparation process. Initially, the peel was thoroughly cleaned with distilled water, and the yellow outer skin was peeled off, revealing the spongy inner skin. Subsequently, the inner skin of grapefruit peel was cut into small squares of 1 × 1 × 1 cm and immersed in a 0.1 mol L^{-1} NaOH solution for 12 hours to facilitate the removal of cellulose. The treated grapefruit peel was repeatedly rinsed with distilled water until a neutral pH was achieved. The grapefruit peel was processed by vacuum freeze-drying and subsequently used for experimental.

The synthesis process began by combining 20 mL of ethanol absolute and a certain volume of tetrabutyl titanate (10 mL, 15 mL, 20 mL, 25 mL) in a round-bottomed flask, with further adjustment of the pH of the solution to 2 *via* acetic acid. Then, 2 g grapefruit peel was added, and the round-bottomed flask containing the solution and grapefruit peel was placed onto a modified rotary evaporator equipped. Maintaining a rotational speed of 180 rpm, the grapefruit peel underwent impregnation through rotation within the mixture for a duration of 12 hours. Finally, it was washed with ethanol absolute until a neutral pH was achieved and was subjected to freeze-drying.

In order to determine the optimal calcination temperature and preparation process parameters, the grapefruit peel loaded

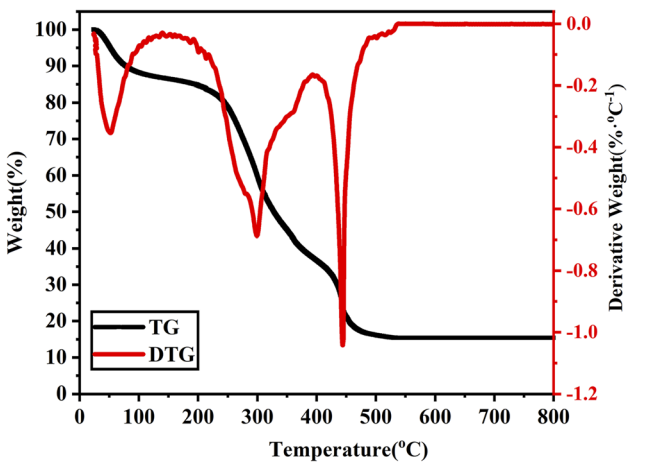

Fig. 1 TG-DTG curves of grapefruit peel loaded with precursors.

Open Access Article. Published on 14 May 2024. Downloaded on 1/20/2026 11:48:06 AM. This article is licensed under a Creative Commons Attribution-NonCommercial 3.0 Unported Licence.

with precursors was first subjected to thermogravimetric analysis (TGA). As shown in Fig. 1, the TG-DTG curve of the grapefruit peel loaded with precursors increased from room to 800 °C at a rate of 5 °C min^{-1} in an air atmosphere. The overall mass loss of the grapefruit peel loaded with precursors was about 85% with the gradual increase of the calcination temperature, and the quality decline mainly experienced three stages. In the first stage, from room temperature to 200 °C, the mass loss was about 15%, mainly caused by the surface adsorption of water and organic volatiles; in the second stage, from 200 °C to 400 °C, the mass loss was about 58%, mainly due to the combustion of organic components in the grapefruit peel; in the third stage, from 400 °C to 530 °C, the mass loss was about 12%, mainly due to the combustion of organic components in the grapefruit peel and the crystallization of titanium dioxide.

To achieve the experimental goal while saving energy, the process parameters of the calcination stage were set as follows: the grapefruit peel loaded with precursor was calcined in a muffle furnace under an air atmosphere, with the temperature rising at a rate of 5 °C min^{-1} from room temperature to 550 °C, followed by a three-hour heat preservation phase, and then naturally cooled to room temperature. According to the added amount of TBOT, the resultant samples were recorded as CPK-TiO_2-x (x = 10, 15, 20, 25). In order to facilitate comparison, control samples without grapefruit peel templates were also prepared under the same conditions, referred to as N-TiO_2-x (x = 10, 15, 20, 25).

2.3 Photocatalytic performance test

Firstly, 100 mL 10 mg L^{-1} RhB solution was measured and poured into a quartz reactor, and 50 mg of photocatalyst powder was then added. The magnetic stirrer was then utilized to disperse the photocatalyst in the dark for 30 minutes. Subsequently, the mercury lamp light source and circulating water cooling device were turned on, and the photocatalytic degradation experiment was conducted. Samples were taken every ten minutes, and the absorbance of the solution was quantified after passing through a 0.45 μm microporous filter membrane. The sampling, filtration, and absorbance steps were repeated until the end of the reaction. The degradation rate was calculated using the mentioned formula. The relationship between C/C_0–t was studied; the degradation rate η was calculated using the following formula:

$$\eta = \frac{C_0 - C}{C_0} \times 100\%$$

where η – degradation rate %, C_0 – dark adsorption equilibrium, starting concentration of pollutant when light is turned on, mol L^{-1}, C – concentration of pollutant after photocatalytic reaction time t, mol L^{-1}.

2.4 Characterization

In this study, a comprehensive set of techniques was utilized to assess the properties of the synthesized material. Thermogravimetric analysis (TGA) was utilized to determine the process parameters of the calcination stage. X-ray diffraction (XRD) was employed to test the crystal structure, X-ray photoelectron spectroscopy (XPS) was employed to assess the elemental composition and the presence of valence states on the surface of the material. SEM and EDS were utilized to assess the microsurface morphology, structure, and elemental distribution. Furthermore, TEM was employed to characterize the microstructure morphology of the materials and to detect the high-resolution lattice fringes and electron diffraction. A fully automated specific surface area analyzer method, BET, was used to analyze the pore size of the materials, and the light absorption properties of the samples were assessed *via* ultraviolet-visible diffuse reflectance spectroscopy (UV-vis DRS). Moreover, the photoluminescence properties were characterized by a fluorescence spectrometer. Using KBr as the reference, the Fourier transform infrared (FTIR) spectrum was used to detect grapefruit peel and the resultant samples. The TOC analyzer was used to test the total organic carbon (TOC) of the pollutants before and after the reaction, and to calculate the mineralization rate. Free radicals were determined by electron paramagnetic resonance spectrometer (EPR).

3 Result and discussion

3.1 Structure of the resulting samples

Fig. 2a depicts the XRD spectra of CPK-TiO_2-x (x = 10, 15, 20, 25) and N-TiO_2-10 samples. From the figure, it can be seen that there are obvious diffraction peaks at about 2θ = 25.32°, 37.86°, 48.06°, 53.97°, 55.09°, 62.75°, 68.87°, 70.33°, and 75.14° for the samples corresponding to (101), (200), (105), (211), (204), (116), (220), and (215) crystal planes, respectively, in the anatase phase of TiO_2 (PDF# 86-1157).[25] Moreover, the absence of other impurity peaks indicates that both CPK-TiO_2-x and N-TiO_2-10 samples exhibit good crystallinity. Notably, the presence of the grapefruit peel template did not impact the crystalline phase structure of TiO_2. According to Scherrer's formula,[26] the average sizes of the crystalline grains can be calculated to be approximately N-TiO_2-10: 25.2 nm, and for samples CPK-TiO_2-x (x = 10, 15, 20, 25), they are 18.12 nm, 20.16 nm, 22.78 nm, 23.01 nm, respectively. It indicated that with the increasing dosages of $Ti(OC_4H_9)_4$, the sizes of the crystalline grains gradually increased.

To precisely assess the changes in crystal cell parameters, Rietveld refinement was performed on the XRD patterns.[27] Fig. 2b displays the Rietveld-refined XRD patterns of N-TiO_2-10 and CPK-TiO_2-10, alongside the experimental patterns and the differential curve. The results, detailed in Table 1, indicate uniform lattice parameters along the a and b axes at 3.785 Å for all samples. Notably, a subtle variation is observed in the c lattice parameter; the c parameter of N-TiO_2-10 is greater than those of CPK-TiO_2-x (x = 10, 15, 20, 25), which incrementally increase with the x value. This suggests that utilizing grapefruit peel as a template in the synthesis of CPK-TiO_2-x (x = 10, 15, 20, 25) induces elemental doping, resulting in the contraction of the lattice parameters in the c-axis orientation of anatase TiO_2.

To enhance comprehension of the structural characteristics associated with the doping process in TiO_2 nanomaterials, X-ray Photoelectron Spectroscopy (XPS) was utilized to analyze the

 © 2024 The Author(s). Published by the Royal Society of Chemistry

Open Access Article. Published on 14 May 2024. Downloaded on 1/20/2026 11:48:06 AM.
This article is licensed under a Creative Commons Attribution-NonCommercial 3.0 Unported Licence.

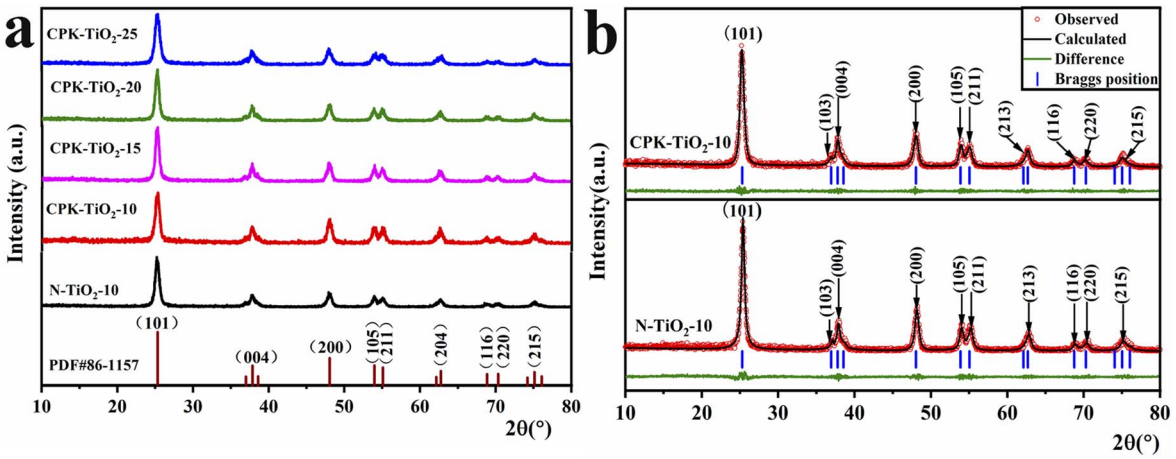

Fig. 2 (a) XRD spectra of CPK-TiO_2-*x* and N-TiO_2-10; (b) Rietveld refined XRD profiles of N-TiO_2-10 and CPK-TiO_2-10.

Table 1 The crystal lattice parameters of TiO_2 were assessed using the Rietveld refinement method

	Lattice parameters			Fitting parameters		
Sample	*a* (Å)	*b* (Å)	*c* (Å)	R_{wp} (%)	R_p (%)	χ^2 (%)
N-TiO_2-10	3.785	3.785	9.509	13.82	10.59	3.69
CPK-TiO_2-10	3.785	3.785	9.494	13.86	10.57	2.47
CPK-TiO_2-15	3.785	3.785	9.497	13.79	10.75	2.38
CPK-TiO_2-20	3.785	3.785	9.501	14.23	10.96	3.82
CPK-TiO_2-25	3.785	3.785	9.503	13.74	10.68	3.57

chemical states and elemental environment. Fig. 3 presents the core-level spectra for Ti 2p, O 1s, C 1s, P 2p, and K 2p; quantitative analysis results are detailed in Table 2. The survey spectrum of the sample (Fig. 3a) reveals that the surface of the CPK-TiO_2-10 and N-TiO_2-10 samples contains primarily elemental compositions of Ti, O, and C. Characteristic peaks of P 2p and K 2p were also observed in the sample CPK-TiO_2-10. Among them, the carbon element may have originated from the environment or the template. The high-resolution XPS spectrum of Ti 2p was analyzed in detail, revealing three distinct peaks (Fig. 3b): Ti $2p_{3/2}$ at 458.5 eV, Ti $2p_{1/2}$ at 464.2 eV, and a satellite peak of Ti near 470.5 eV, which are characteristic values of Ti^{4+}.[28] This indicates the formation of TiO_2. The high-resolution XPS spectrum of O 1s depicts distinct peaks for both CPK-TiO_2-10 and N-TiO_2-10 (Fig. 3c). The O 1s orbital XPS spectrum of the N-TiO_2-10 sample can be fitted to two peaks with binding energies of 529.68 eV and 532.50 eV corresponding

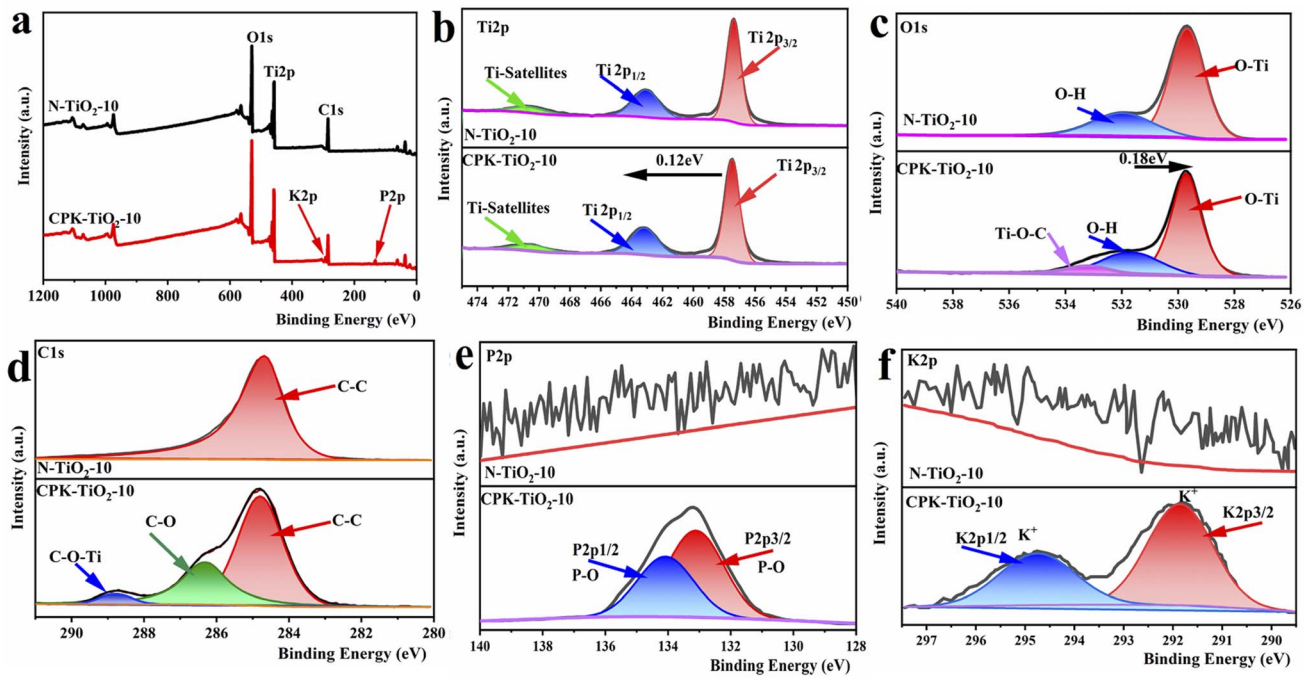

Fig. 3 X-ray energy spectrum of CPK-TiO_2-10 and N-TiO_2-10 (a) XPS survey spectrum; High-resolution XPS spectra of (b) Ti 2p, (c) O 1s, (d) C 1s, (e) P 2p and (f) K 2p.

Open Access Article. Published on 14 May 2024. Downloaded on 1/20/2026 11:48:06 AM.
This article is licensed under a Creative Commons Attribution-NonCommercial 3.0 Unported Licence.

Table 2 Binding energy and atomic elemental concentration evaluated from XPS spectra of CPK-TiO_2-10

Element	BE/ev	Group	At%	
Ti 2p	464.15	Ti–O	13.32	17.78
	458.46	Ti–O	4.26	
O 1s	529.71	O–Ti	26.83	47.37
	530.92	O–H	13.26	
	532.62	C–O–Ti, P–O–Ti, O–C–O	7.28	
C 1s	284.80	C–C	21.28	33.29
	286.29	C–O	10.68	
	288.77	C–O–Ti	1.33	
P 2p	133.28	P–O	0.67	1.09
	134.38	P–O	0.42	
K 2p	291.87	K^+	0.31	0.47
	294.72	K^+	0.16	

to O–Ti bonds (lattice oxygen) and O–H (adsorbed oxygen), respectively.[29] Moreover, in the CPK-TiO_2-10 sample, the O 1s orbital XPS spectrum can be fitted to three peaks. Alongside the O–Ti bond (lattice oxygen) with a binding energy of 529.68 eV and O–H (adsorbed oxygen) at 532.50 eV, there is an additional peak at 531.15 eV, corresponding to Ti–O–C. This implies that there may be a trace amount of carbon incorporated into the lattice of TiO_2.

Fig. 3d depicts the high-resolution XPS spectra of the C 1s orbitals of the samples CPK-TiO_2-10 and N-TiO_2-10. For N-TiO_2-10, a single peak at a binding energy of 284.80 eV corresponds to only C–C, indicating adsorbed carbon from the environment. The C 1s in CPK-TiO_2-10 were fitted as three peaks. Similar to N-TiO_2-10, the binding energy at 284.80 eV and 286.60 eV of CPK-TiO_2-10 are attributed to adsorbed environmental carbon and carbon contamination introduced during testing.[30] Another peak was observed at 288.77 eV, where the C may originate from a small amount of carbon residue in the template of grapefruit peel, forming C–O–Ti bonds, successfully incorporated into the lattice of TiO_2. This is confirmed by the O 1s peak at 531.15 eV, indicating the substitution of Ti atoms by C, forming Ti–O–C structure and leading to lattice contraction in TiO_2. Additionally, no peak was detected around 282 eV, indicating the absence of Ti–C bonds generated by the substitution of oxygen atoms with carbon atoms.[31] Fig. 3e depicts the high-resolution XPS spectra of the P 2p orbitals of the samples CPK-TiO_2-10 and N-TiO_2-10. The characteristic peak of P 2p was not observed in sample N-TiO_2-10. In the sample CPK-TiO_2-10, the P 2p spectra can be distinctly seen, with peaks at 133.11 eV and 134.07 eV corresponding to the typical P–O bond. This indicates that a small amount of P^{5+} may replace Ti^{4+} to form Ti–O–P bonds or to form PO_4^{3-} on the surface of TiO_2. Furthermore, the absence of a peak at 129 eV in the P 2p region suggests that no Ti–P bond is formed.[32] Fig. 3f shows the high-resolution XPS spectra of the K 2p orbitals for the samples CPK-TiO_2-10 and N-TiO_2-10. The characteristic peak of K 2p was not detected in sample N-TiO_2-10. However, in sample CPK-TiO_2-10, distinct K 2p spectra are visible, with peaks at 292.2 eV and 294.5 eV corresponding to the K $2p_{1/2}$ and K $2p_{3/2}$ orbitals.[33] This indicates that K exists in the sample in the form of K^+. The XPS tests demonstrate that C, P, K elements self-doped into TiO_2 from grapefruit peel.

Fig. 4a depicts the nitrogen adsorption–desorption isotherms of CPK-TiO_2-x (x = 10, 15, 20, 25) and N-TiO_2-10 samples. Fig. 4a reveals that according to the classification rules of IUPAC,[34] the nitrogen adsorption–desorption isotherms of CPK-TiO_2-x (x = 10, 15, 20, 25) and N-TiO_2-10 samples belong to type IV. The CPK-TiO_2-x (x = 10, 15, 20) samples exhibit obvious H3-type migratory hysteresis loops in the nitrogen adsorption–desorption isotherms, indicating that the CPK-TiO_2-x (x = 10, 15, 20) samples have a typical mesoporous structure with abundant pores. However, the H_3 migratory hysteresis loop in the nitrogen adsorption–desorption isotherm of the CPK-TiO_2-25 and N-TiO_2-10 samples are very small, implying the relatively less porous structure of the CPK-TiO_2-25 and N-TiO_2-10 samples.

Fig. 4b depicts the distribution of the pore sizes of CPK-TiO_2-x (x = 10, 15, 20, 25) and N-TiO_2-10 samples. The figure exhibits two peaks in the CPK-TiO_2-10 (x = 10, 15, 20) samples, which indicates that the pore size of CPK-TiO_2-x (x = 10, 15, 20)

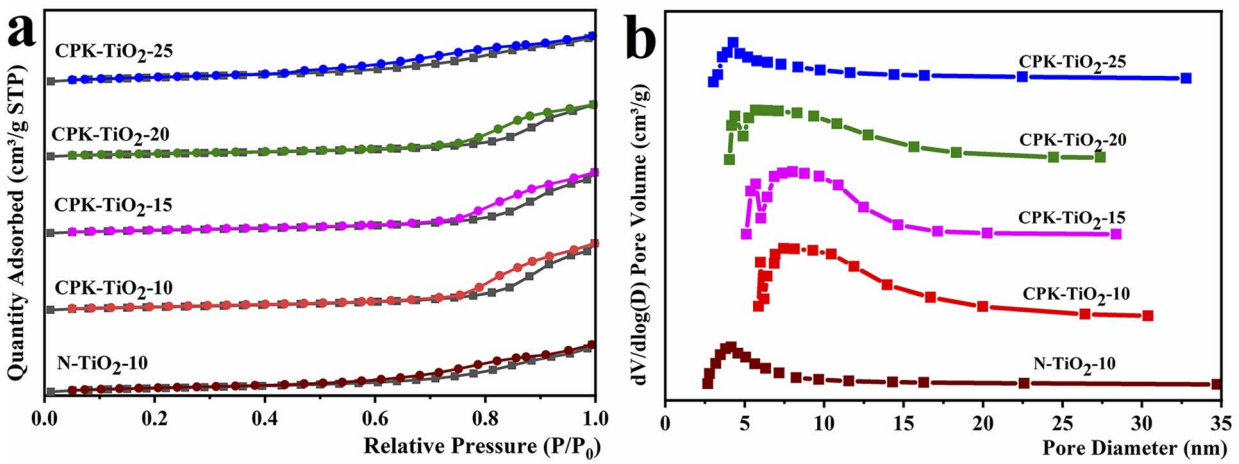

Fig. 4 (a) N_2 adsorption–desorption isotherms; (b) pore size distributions of CPK-TiO_2-x (x = 10, 15, 20, 25) and N-TiO_2-10.

© 2024 The Author(s). Published by the Royal Society of Chemistry

Open Access Article. Published on 14 May 2024. Downloaded on 1/20/2026 11:48:06 AM.
This article is licensed under a Creative Commons Attribution-NonCommercial 3.0 Unported Licence.

Table 3 Surface area, pore volume, and pore diameter distribution of CPK-TiO_2-x (x = 10, 15, 20, 25) and N-TiO_2-10

Materials	BET surface area (m^2 g^{-1})	Pore volume (m^3 g^{-1})	Pore diameter (nm)
N-TiO_2-10	38.89	0.11	8.9
CPK-TiO_2-10	79.80	0.28	12.1
CPK-TiO_2-15	62.54	0.24	10.8
CPK-TiO_2-20	56.73	0.21	9.6
CPK-TiO_2-25	49.42	0.18	9.2

samples is not uniform. It is primarily distributed between 3.0 nm and 20.0 nm, which is characteristic of mesopores. This may be due to the existence of the voids in the material itself and the slits between the nanoparticles, which are not uniform. Consequently, the pore size distribution exists in two regions. The pore size of CPK-TiO_2-25 and N-TiO_2-10 is primarily distributed between 3.0 nm and 15.0 nm, also belonging to mesopores, possibly attributed to stacking pores between TiO_2 particles.

The surface areas, pore volumes, and average pore diameters of CPK-TiO_2-x (x = 10, 15, 20, 25) and N-TiO_2-10 samples are depicted in Table 3. It can be seen that with the increased dosages of TBOT, the surface areas, pore volumes, and average pore diameters were all decreased.

Among them, the sample of CPK-TiO_2-10 has the largest surface area and the sample of N-TiO_2-10 has the smallest surface area. The surface areas of CPK-TiO_2-10 and N-TiO_2-10 were noted at 79.80 m^2 g^{-1} and 38.89 m^2 g^{-1}, respectively. The surface area of CPK-TiO_2-10 is approximately 2 times the surface area of N-TiO_2-10. Furthermore, the pore volumes of CPK-TiO_2-10 and N-TiO_2-10 were observed at 0.28 m^3 g^{-1} and 0.11 m^3 g^{-1}, and the average pore sizes of CPK-TiO_2-10 and N-TiO_2-10 were noted at 12.1 nm and 8.9 nm, respectively. This indicates that CPK-TiO_2-10 possesses a larger number of active sites, which can effectively promote the photocatalytic reaction.[34,35] Therefore, the sample of CPK-TiO_2-10 has the potential advantage of becoming a good photocatalytic material.

3.2 Morphology of the resulting samples

In order to investigate the influence of the dosage of TBOT on the morphology and structure of the products, SEM tests were conducted on the samples CPK-TiO_2-x (x = 10, 15, 20, 25), and the results are depicted in Fig. 5. The illustration in Fig. 5 depicts the particle size distribution of the sample. Fig. 5 shows that the samples CPK-TiO_2-x (x = 10, 15, 20, 25) consist of spherical-like nanoparticles with a wrinkled surface. As the TBOT dosage increases from 10 mL to 25 mL, the nanoparticle size gradually increases, measuring between 17 nm and 23 nm for samples CPK-TiO_2-x (x = 10, 15, 20, 25). Particle aggregation intensifies, leading to pore blockage. A smaller TBOT dosage reduces particle size, increasing surface area and pore abundance. However, yields are low when TBOT added is below 10 mL. Therefore, adding 10 mL of TBOT is recommended.

In order to study the influence of the template on the morphology and structure of the product, we selected grapefruit peel and sample CPK-TiO_2-10 for SEM detection, and the results are shown in Fig. 6.

Fig. 6a_1 depicts that the grapefruit peel exhibits a porous structure formed by interlinked curled layers, with a layer thickness ranging from approximately 5 μm to 7 μm. In order to further investigate the morphology and structure of the grapefruit peel fibers, the image of Fig. 6a_1 was further magnified. From Fig. 6a_2, it can be seen that the surface of grapefruit peel fibers is relatively smooth and wrinkled. Further magnification, as shown in Fig. 6a_3, reveals that the surface of grapefruit peel fibers has a rich pore structure. This intricate structure indicates a substantial internal storage space within the grapefruit

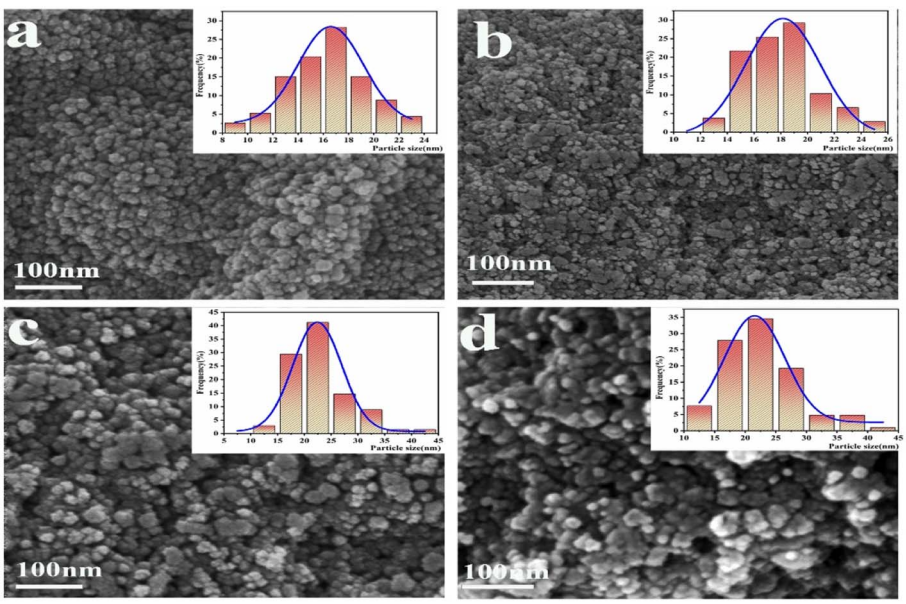

Fig. 5 SEM images of the CPK-TiO_2-10 (a), CPK-TiO_2-15 (b), CPK-TiO_2-20 (c), CPK-TiO_2-25 (d).

Open Access Article. Published on 14 May 2024. Downloaded on 1/20/2026 11:48:06 AM.
This article is licensed under a Creative Commons Attribution-NonCommercial 3.0 Unported Licence.

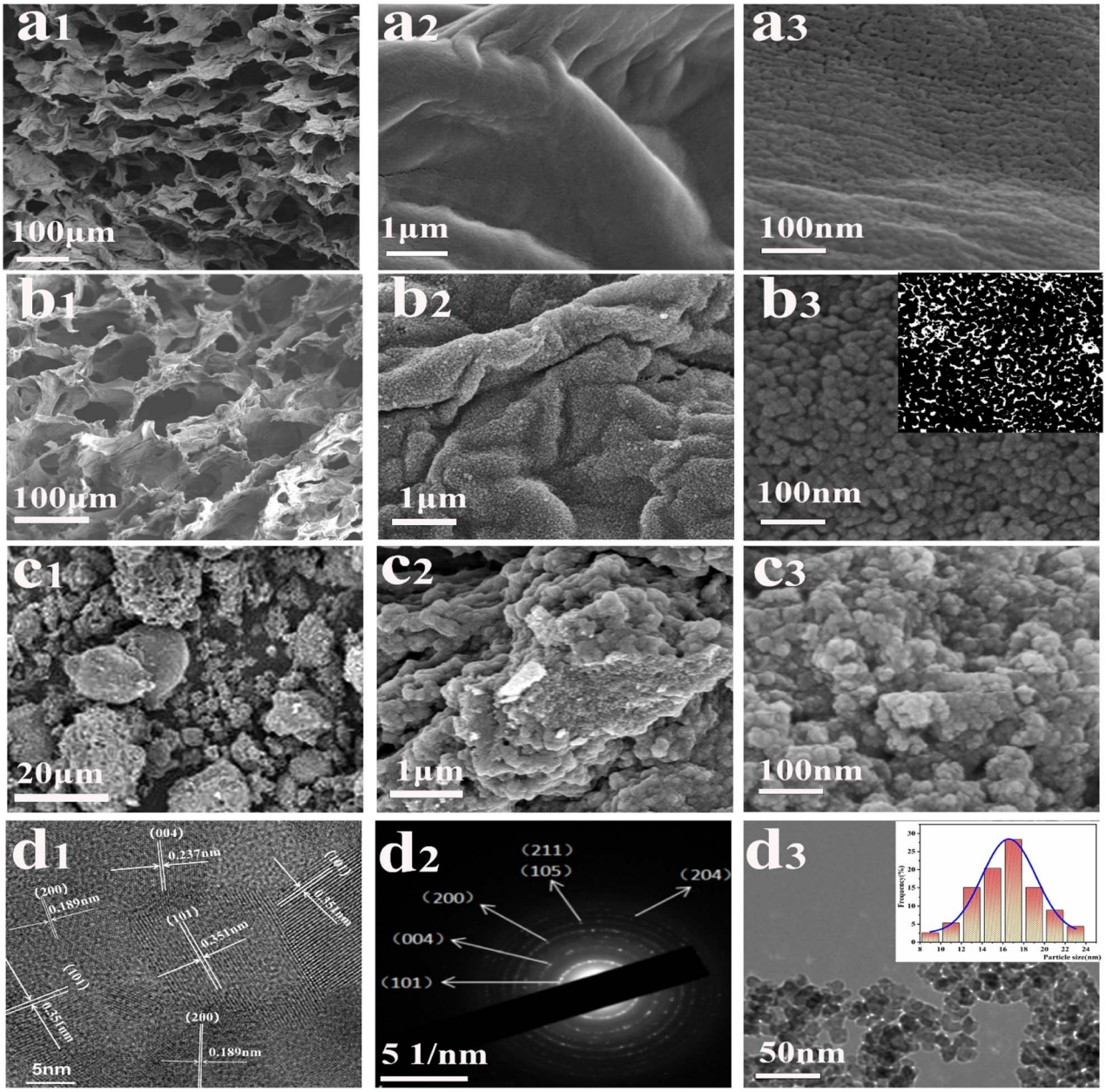

Fig. 6 SEM images of grapefruit peel (a_1–a_3), CPK-TiO_2-10 (b_1–b_3), N-TiO_2-10 (c_1–c_3); HRTEM image (d_1), selected area electron diffraction (d_2), and TEM images (d_3) of CPK-TiO_2-10.

peel, suggesting its potential as a biological template for the preparation of inorganic porous materials.

Fig. 6b_1 demonstrates that the sample CPK-TiO_2-10 perfectly replicates the original biological morphology of the grapefruit peel, forming a porous structure composed of interconnected layered structures. Further magnification of the SEM image (Fig. 6b_2 and b_3) reveals that the sample CPK-TiO_2-10 is assembled layer by layer from spherical-like nanoparticles along the grapefruit peel fibers, with a wrinkled surface and abundant pores formed by the assembly of particles. The illustration in Fig. 6b_3 shows voids identified in SEM images analyzed with ImageJ software; the white areas indicate voids, and the porosity is estimated to be approximately 21.42%

From the SEM image of the control sample N-TiO_2-10 (Fig. 6c_1–c_3), it can be observed that the sample N-TiO_2-10 has an irregular shape and is composed of spherical particles with uneven particle size and obvious agglomeration phenomenon.

To further investigate the microstructure of the material, the sample CPK-TiO_2-10 was analyzed by HRTEM, and the results are shown in Fig. 6d_1–d_3. The high-resolution transmission electron micrograph image of the CPK-TiO_2-10 sample in Fig. 6d_1 exhibits various clear lattice stripes. Their lattice spacings are measured to be 0.351 nm, 0.189 nm, and 0.237 nm, which correspond to the (101), (200), and (004) crystalline planes of TiO_2, respectively.[35] This data aligns with the XRD characterization results. The selected area electron

© 2024 The Author(s). Published by the Royal Society of Chemistry

Open Access Article. Published on 14 May 2024. Downloaded on 1/20/2026 11:48:06 AM.
This article is licensed under a Creative Commons Attribution-NonCommercial 3.0 Unported Licence.

diffractogram (SAED) image of the CPK-TiO_2-10 sample in Fig. 6d$_2$ reveals that the SAED consists of typical polycrystalline diffraction rings. It indicates that the sample CPK-TiO_2-10 has a polycrystalline structure with good crystallinity. The TEM image of CPK-TiO_2-10 (Fig. 6d$_3$) reveals that the CPK-TiO_2-10 comprises a stack of small particles, with the interparticle pores clearly observable. The particle size distribution diagram (Fig. 6d$_3$, inset) shows that the average particle size of CPK-TiO_2-10 is approximately 17 nm, demonstrating uniformity. This measurement aligns closely with the values obtained from XRD analysis using the Scherrer formula.

Fig. 7a–f depicts the elemental distribution of CPK-TiO_2-10. It was observed that the elements Ti, O, C, P, and K in the CPK-TiO_2-10 sample are uniformly distributed throughout the area. The EDS energy spectrum of N-TiO_2-10 (Fig. 7g) shows that the atomic number percentage contents of Ti and O in this sample are 32.64% and 67.36%, respectively, and there are no other impurity elements, affirming its composition as TiO_2.The EDS energy spectrum of CPK-TiO_2-10 (Fig. 7h) reveals that the atomic number percentage contents of Ti, O, C, P, and K in this sample are 23.47%, 69.61%, 5.09%, 1.26%, and 0.57%, respectively, which further confirms that the elements C, P, K in the grapefruit peel are doped into the TiO_2. Combining XRD spectra (Fig. 2) and XPS spectra (Fig. 3) can demonstrate that C, P, K elements self-doped into TiO_2 from grapefruit peel.

3.3 Synthesis mechanism of the prepared CPK-TiO_2

To investigate the organic functional groups on the surface of grapefruit peel template and their roles in the formation of CPK-TiO_2, infrared spectra analysis was conducted on grapefruit peel (GP), intermediate product (grapefruit peel soaked in precursor solution, dried but not yet calcined) (GPT), and sample CPK-TiO_2-10, as shown in Fig. 8.

The FTIR spectra of grapefruit peel (Fig. 8a) show a strong and broad characteristic peak around 3432 cm^{-1}, attributed to the stretching vibration of O–H bonds.[36] There is a saturated alkane stretching vibration absorption peak around 2920 cm^{-1}, and C=O stretching vibration absorption peaks are observed near 1754 cm^{-1} and 1625 cm^{-1}.[36,37] The absorption peaks at 1383 cm^{-1} and 1054 cm^{-1} are caused by the stretching vibrations of C–C and C–O–C bonds.[37] Analysis of the FTIR spectra of grapefruit peel reveals that the surface of grapefruit peel contains abundant oxygen-containing functional groups. These oxygen-containing groups assist in anchoring titanium sources during the impregnation process. The FTIR spectra of the intermediate product (Fig. 8b) indicate that the hydroxyl absorption peak at 3448 cm^{-1} has undergone a redshift relative to the grapefruit peel, and the absorption peak at 2920 cm^{-1} has disappeared. This is attributed to chemical reactions between Ti^{4+} in TBOT and hydroxyl, carbonyl, and other organic functional groups on the surface of grapefruit peel during the

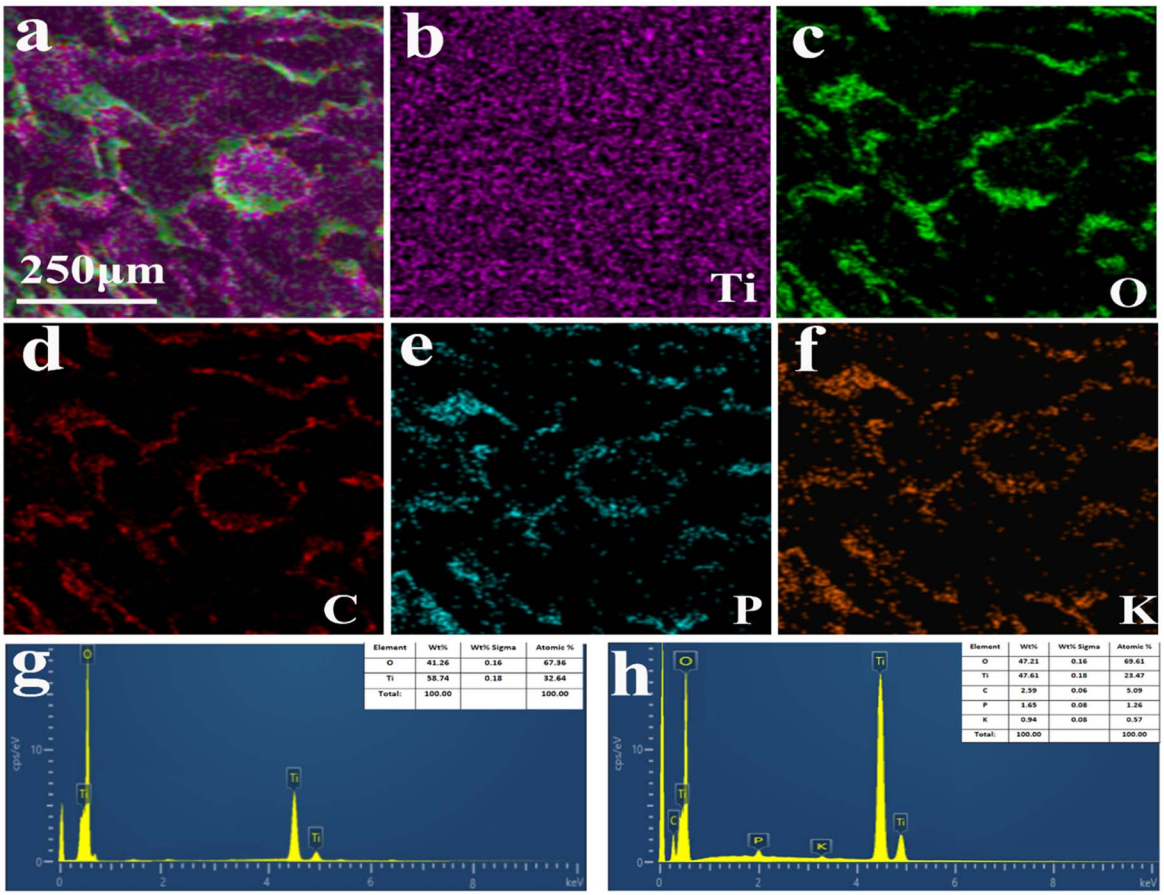

Fig. 7 EDS elemental distribution of CPK-TiO_2-10 (a–f) and EDS energy spectrum of CPK-TiO_2-10 (g) and N-TiO_2-10 (h).

Open Access Article. Published on 14 May 2024. Downloaded on 1/20/2026 11:48:06 AM.
This article is licensed under a Creative Commons Attribution-NonCommercial 3.0 Unported Licence.

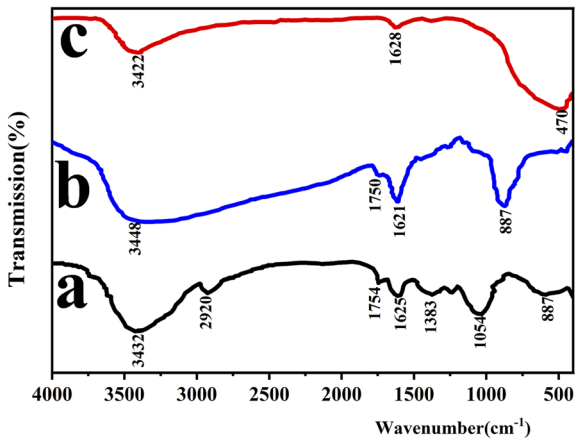

Fig. 8 FTIR spectra of GP (a), GPT (b) and CPK-TiO_2-10 (c).

impregnation process, resulting in changes in the functional groups on the surface of the grapefruit peel. The FTIR spectra of sample CPK-TiO_2-10 (Fig. 8c) show a distinctive absorption peak near 470 cm^{-1}, which, as reported in the literature, is attributed to the stretching vibration of the Ti–O bond and the bridging stretching vibration of the Ti–O–Ti bond.[38] This indicates the successful preparation of TiO_2. Additionally, the absorption peaks around 1628 cm^{-1} and 3422 cm^{-1} correspond to the stretching and bending vibrations of hydroxyl groups, which may be due to the adsorption of water or residual hydroxyl groups on the sample surface.

Scheme 1 exhibits the formation of CPK-TiO_2. From the FTIR spectra analysis, we know that it is rich in O–H groups, C=O groups, and C–H groups on the surface of GP. The interaction between the Ti^{4+} of TBOT and the organic functional groups of the grapefruit peels was either electrostatically attracted or chemically bonded, resulting in the formation of $Ti(OC_4H_9)_4$/GP when immersed in an ethanol solution of TBOT. The hydrolysis of tetrabutyl titanate leads to the formation of $Ti(OH)_4$/GP on the surface of grapefruit peels. When this material is calcined at high temperatures in an air atmosphere, $Ti(OH)_4$ will decompose, and titanium dioxide will undergo *in situ* nucleation and growth along the direction of the grapefruit peel fiber.

At high temperatures, the major elements such as C and N in the bio-template will undergo combustion, producing CO_2 leading to the gradual disappearance of the template. TiO_2 nanoparticles will then assemble into a porous structure guided by the bio-template. Meanwhile, elements such as P and K that do not combust at high temperatures, along with residual C elements, will be doped into the TiO_2.

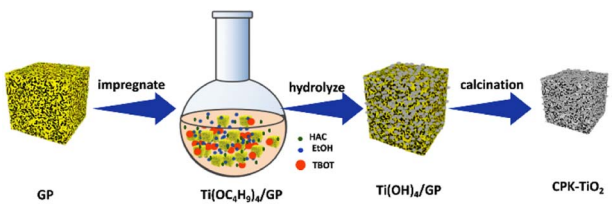

Scheme 1 Schematic presentation of the formation of the CPK-TiO_2.

3.4 Analysis of the optical properties of the resulting samples

To examine the light absorption properties of the samples, UV-vis DRS was utilized to assess the CPK-TiO_2-x (x = 10, 15, 20, 25) and N-TiO_2-10 samples and to calculate their band gaps. Fig. 9a reveals that the UV-vis DRS of CPK-TiO_2-x (x = 10, 15, 20, 25) and N-TiO_2-10 are very similar, with notable absorption in the UV region of 200–400 nm. The N-TiO_2-10 sample absorption is negligible, whereas the CPK-TiO_2-x (x = 10, 15, 20, 25) samples have weak absorption in the visible region of 400–800 nm. However, the absorption band edges of the CPK-TiO_2-x samples were redshifted with respect to N-TiO_2-10. The absorption band edges of N-TiO_2-10 were approximately 387 nm, whereas those of CPK-TiO_2-x were approximately 403 nm. In addition, the light absorption intensity of CPK-TiO_2-x (x = 10, 15, 20, 25) gradually decreases with the increase dosages of TBOT, which should be related to the samples' structure. The larger the surface area of the sample, the more favorable the light absorption. From Table 3, we can see that the surface area of CPK-TiO_2-x (x = 10, 15, 20, 25) samples decreases from 79.80 $m^2\ g^{-1}$ to 49.42 $m^2\ g^{-1}$ with the increased dosages of TBOT. Thus, the CPK-TiO_2-10 sample has the strongest light absorption potential. The band gaps of the CPK-TiO_2-10 and N-TiO_2-10 samples were computed using Tauc plots[39] to be 3.076 eV and 3.201 eV, respectively (Fig. 9b). The reduction in the band gap of the TiO_2 samples may be attributed to the doping of small amounts of C, P, and K elements, which alter the crystal structure or introduce dopant energy levels into TiO_2's energy bands. Additionally, a decrease in particle size also contributes to band gap changes. These modifications expand the photoresponse range and enhance the photocatalytic capabilities of the samples.

The fluorescence emission spectrum is commonly used to study the separation efficiency of photogenerated electrons and holes in photocatalysts. The fluorescence intensity serves as an indicator of the compounding probability of photogenerated electron–hole pairs, where higher intensity suggests lower separation efficiency, correlating with reduced photocatalytic activity, and *vice versa*.[40] Fluorescence spectrum tests were carried out on CPK-TiO_2-x (x = 10, 15, 20, 25) and N-TiO_2-10, respectively, with an excitation wavelength of 320 nm.[41] The resulting data, depicted in Fig. 9c, reveals that under the excitation of 320 nm light, PL emission peaks appeared near 420 nm for both CPK-TiO_2-x and N-TiO_2-10 samples with similar spectra. However, the emission intensity of CPK-TiO_2-x (x = 10, 15, 20, 25) is lower than that of the N-TiO_2-10 sample. Moreover, the emission intensity of the samples CPK-TiO_2-x (x = 10, 15, 20, 25) gradually strengthens with increasing dosages of TBOT. Among these samples, the sample CPK-TiO_2-10 has the lowest fluorescence intensity, which indicates that the sample CPK-TiO_2-10 has a lower compounding probability of photogenerated electron–hole pairs and higher separation efficiency than the other samples. This observation suggests that the sample CPK-TiO_2-10 will exhibit better photocatalytic activity. The influence of biological C, P, K doping from grapefruit peel is hypothesized to contribute to this effect, as the introduction of C, P, K greatly restricts the compounding of the photogenerated

© 2024 The Author(s). Published by the Royal Society of Chemistry

Open Access Article. Published on 14 May 2024. Downloaded on 1/20/2026 11:48:06 AM.
This article is licensed under a Creative Commons Attribution-NonCommercial 3.0 Unported Licence.

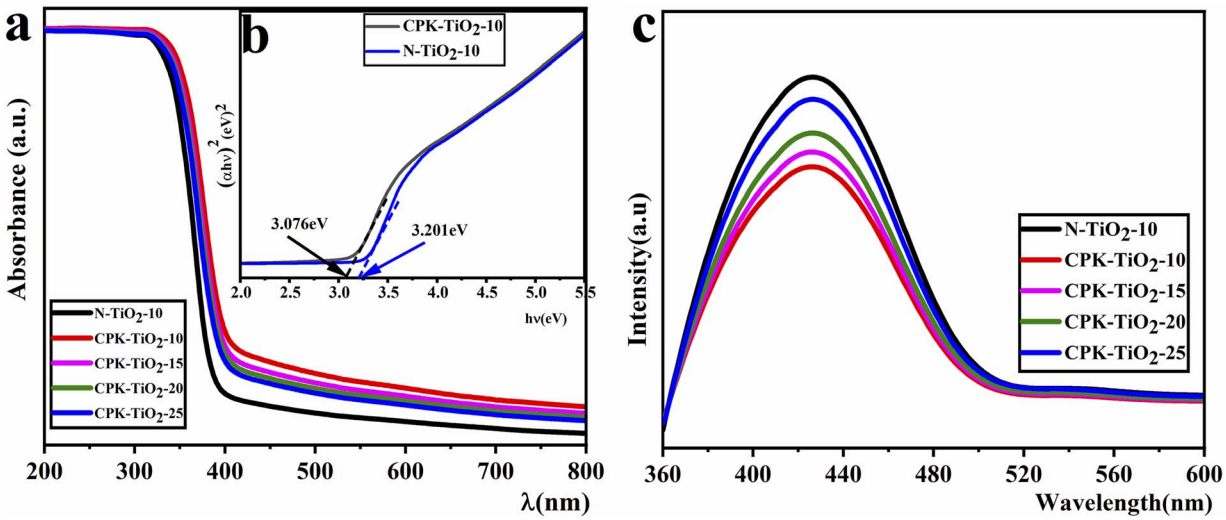

Fig. 9 UV-visible diffuse reflectance absorption spectra (a), band gap energy spectra (b), and fluorescence spectrum (c) of CPK-TiO_2-x (x = 10, 15, 20, 25) and N-TiO_2-10 samples.

electron–hole pairs. Consequently, the CPK-TiO_2-10 sample has a very high separation efficiency of the photogenerated electron–hole pairs, leading to heightened photocatalytic activity. This observation aligns with the trend of the redshift of the absorption edge of the UV-vis DRS spectra.

3.5 Analysis of photocatalytic performance in the resulting samples

Assessing the photocatalytic degradation performance of CPK-TiO_2-x (x = 10, 15, 20, 25) samples on dyeing wastewater involved selecting N-TiO_2-10 and P25 (commercial TiO_2 with an average particle size of 25 nm) as references, and RhB served as the model pollutant for the photocatalytic experiments. The experimental conditions were as follows: the initial concentration of RhB was 10 mg L^{-1}, determined by the untreated dyeing wastewater concentration in the factory (approximately 10–20 mg L^{-1}).[41] The RhB solution volume was 100 mL, with a photocatalyst addition of 50 mg/100 mL. The reaction was conducted at a temperature of 25 °C, an initial pH of around 4.9 (original), and a 300 W mercury lamp served as the light source. The results are depicted in Fig. 10.

From Fig. 10a, we can see that despite the exposure to a 300 W mercury lamp for 60 minutes, the degradation rate of RhB remained minimal without the presence of photocatalysts. This suggests the relative stability of RhB under light, with negligible photodegradation, making it suitable as a simulated pollutant for photocatalytic degradation experiments. The adsorption rates of N-TiO_2-10 and P25 samples for RhB solution in the dark were extremely low, each being lower than 3%. The adsorption rates of CPK-TiO_2-x (x = 10, 15, 20, 25) samples decrease from 14.3% to 5.9% with increasing dosages of $Ti(OC_4H_9)_4$. Following 60 minutes of light exposure, the degradation rates of RhB by P25 and N-TiO_2-10 were 86.36% and 78.09%, respectively. The degradation rates of CPK-TiO_2-x (x = 10, 15, 20, 25) samples were 100%, 98.52%, 95.06%, 92.76%, respectively. CPK-TiO_2-x (x = 10, 15, 20, 25) samples exhibited superior photocatalytic degradation of RhB solution compared to N-TiO_2-10 and P25, and the photocatalytic activity of the CPK-TiO_2-x samples gradually decreases with increasing dosages of $Ti(OC_4H_9)_4$. It can be seen that the CPK-TiO_2-10 sample has the best ability to photocatalytically degrade the RhB solution.

To further investigate the performance of CPK-TiO_2-x (x = 10, 15, 20, 25), N-TiO_2-10, and P25 in degrading RhB solution, the kinetic degradation curves of photocatalytic degradation were plotted. The horizontal axis denotes time, and the vertical axis denotes $\ln(C_0/C)$. The corresponding results are depicted in Fig. 10b. The figure reveals that during the photocatalytic degradation of the RhB solution, the kinetic degradation curves for CPK-TiO_2-x (x = 10, 15, 20, 25), N-TiO_2-10, and P25 samples all conformed to the pseudo-first-order kinetic model, demonstrating strong correlations with linear correlation coefficients (R^2) exceeding 0.99. The degradation rate constants k for RhB are as follows: 0.0331 min^{-1} for P25, 0.0251 min^{-1} for N-TiO_2-10, 0.0651 min^{-1} for CPK-TiO_2-10, 0.0604 min^{-1} for CPK-TiO_2-15, 0.0500 min^{-1} for CPK-TiO_2-20, and 0.0441 min^{-1} for CPK-TiO_2-25, respectively. This indicates that the catalytic degradation of organic pollutants under UV light by CPK-TiO_2-x (x = 10, 15, 20, 25) samples is markedly better than that of N-TiO_2-10 and P25 samples. Among these samples, the CPK-TiO_2-10 sample has the best photocatalytic performance.

This superiority can be attributed to the gradient porous mesh structure of the CPK-TiO_2-10 sample, featuring abundant pores and a larger surface area. According to the literature, photocatalytic materials with larger surface areas are more conducive to the contact between catalyst and contaminant and promote the transfer and transportation of reactants and products.[42] In addition, the CPK-TiO_2-10 sample has the highest photogenerated electron–hole separation efficiency. Consequently, the CPK-TiO_2-10 sample has the best photocatalytic performance. N_2 adsorption–desorption isotherms (Fig. 4a), pore size distributions (Fig. 4b), surface area distribution, pore

Open Access Article. Published on 14 May 2024. Downloaded on 1/20/2026 11:48:06 AM.
This article is licensed under a Creative Commons Attribution-NonCommercial 3.0 Unported Licence.

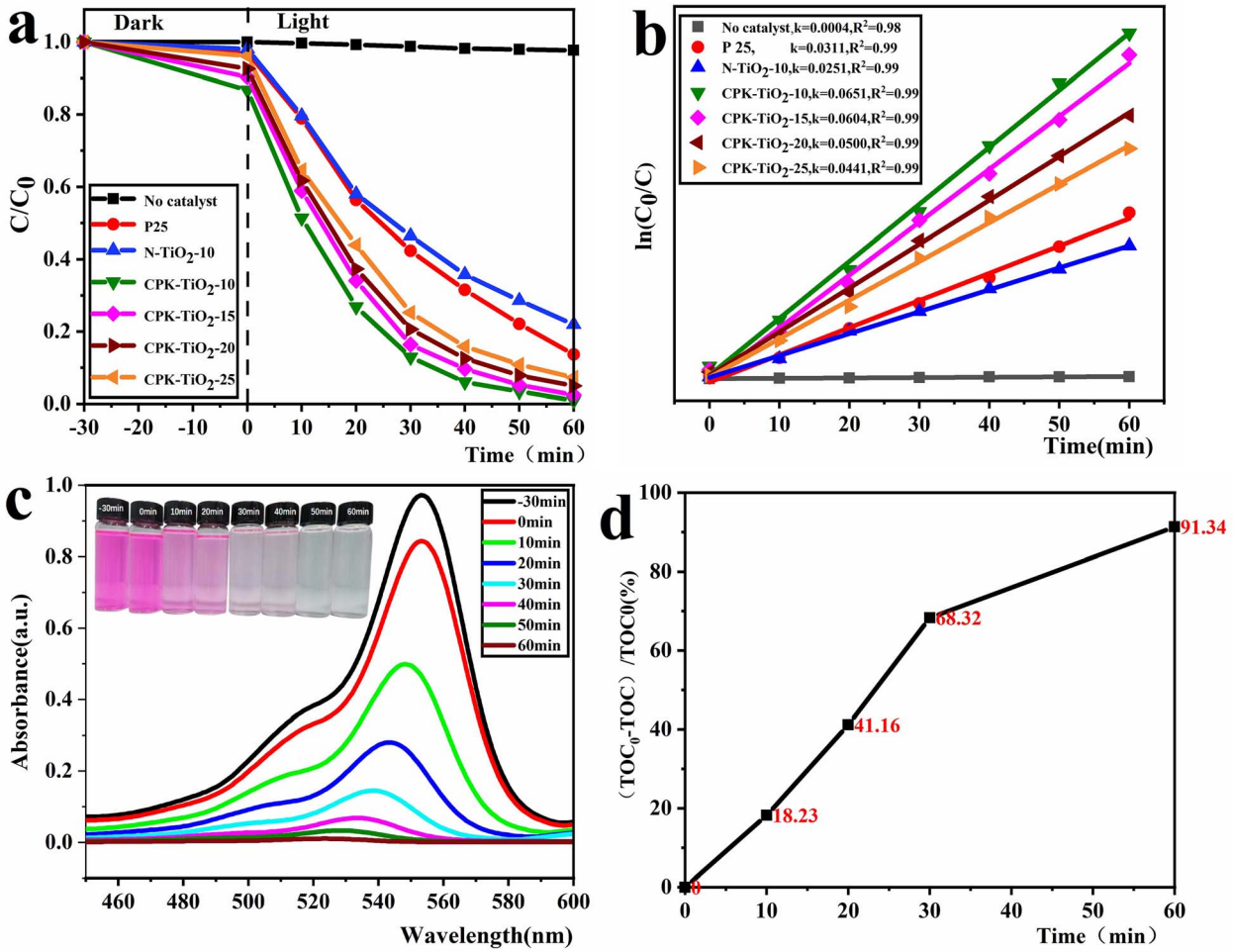

Fig. 10 The photocatalytic degradation curves (a) and kinetic curves (b) by CPK-TiO_2-x (x = 10, 15, 20, 25), N-TiO_2-10, P25, and without catalysis are presented. The photocatalytic degradation spectra (c) and mineralization (d) by CPK-TiO_2-10 for RhB under 300 W mercury lamp irradiation.

volume distribution, and pore diameter distribution (Table 3) and fluorescence spectrum (Fig. 9c) of the samples can provide data to support the above reasoning.

Fig. 10c depicts the spectra of the CPK-TiO_2-10 sample during photocatalytic degradation of RhB dye solution at various reaction times and the corresponding changes in solution color. The figure reveals that the color of the RhB solution gradually fades and the intensity of the characteristic peak at 554 nm in the RhB solution becomes gradually weaker as the reaction time increases. Generally, it is believed that the characteristic absorption peak at 554 nm in the RhB solution is generated by the chromophore of the aromatic ring in the molecular structure of RhB.[43] The weakening and disappearance of the characteristic absorption peaks indicate that the aromatic ring structures in the RhB dye molecules are destroyed. This suggests that the CPK-TiO_2-10 sample not only eliminates the color of the RhB solution but also destroys its organic structure.

To further investigate the mineralization efficiency of the RhB solution with CPK-TiO_2-10, the TOC of the RhB solution was measured using a TOC analysis instrument. The resulting data is depicted in Fig. 10d. According to the figure, the TOC removal efficiency of the RhB solution is 68.32% in 30 min, and 91.34% in 60 min. It suggests that the CPK-TiO_2-10 sample not only decolorized the RhB solution but also deeply mineralized it under ultraviolet light.

3.6 Analysis of cycling stability in the tested samples

The cycling stability of photocatalysts is an important indicator for their application performance. Hence, the cycling stability of CPK-TiO_2-10 was evaluated. The cycle experiments were conducted as follows: after each reaction, the CPK-TiO_2-10 was recovered by centrifugation and dried. Furthermore, the same experimental conditions were maintained throughout. The results are depicted in Fig. 11.

Fig. 11a exhibits the degradation of the RhB solution in five cycle experiments. We can see that the adsorption rate of RhB decreases from 14.3% to 2.7% in 30 minutes, and the degradation rate of RhB decreases from 99.88% to 87.79% after five cycles. The decrease in adsorption rate is likely due to the blockage or destruction of the pore structure of the sample by RhB dye molecules or their degradation products. The decrease in degradation rate after five cycles of reuse may be related to

© 2024 The Author(s). Published by the Royal Society of Chemistry

Open Access Article. Published on 14 May 2024. Downloaded on 1/20/2026 11:48:06 AM.
This article is licensed under a Creative Commons Attribution-NonCommercial 3.0 Unported Licence.

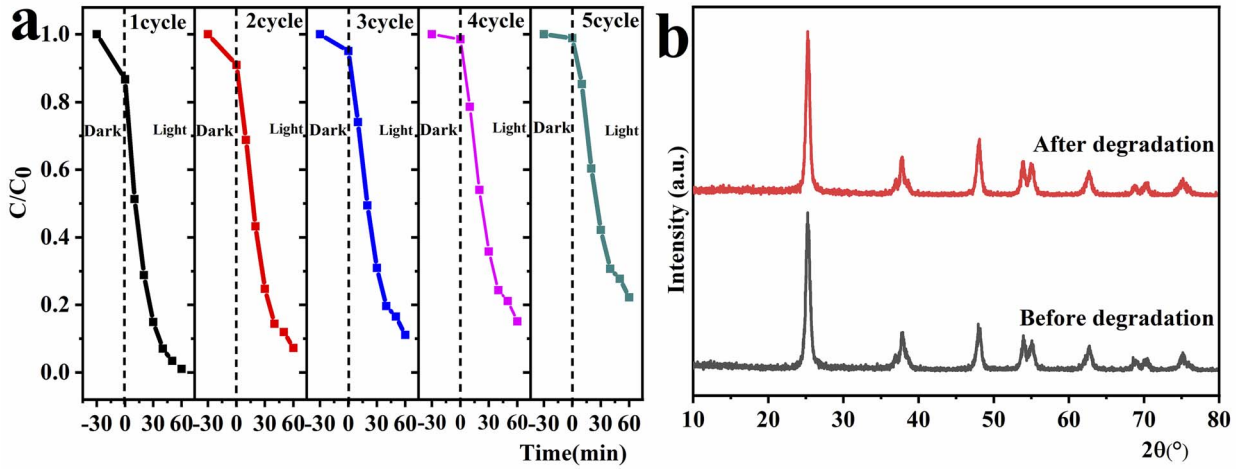

Fig. 11 Cycling runs of degradation for RhB (a), XRD pattern of CPK-TiO_2-10 before and after the degradation process (b).

the loss of catalyst. When measuring the absorbance, a small amount of the CPK-TiO_2-10 catalyst was filtered out of the solution using a microporous filter membrane. Additionally, a small amount of catalyst was lost during the washing process with distilled water following the separation of the catalyst in each cycle of the experiment.

In addition, XRD characterization analysis of the CPK-TiO_2-10 sample before and after the cycling experiments was performed, as depicted in Fig. 11b. The figure shows that no new diffraction peaks appeared in the XRD spectra of CPK-TiO_2-10 after five consecutive cycling reactions, indicating the absence of new phases. The results highlight the excellent cycling stability of the CPK-TiO_2-10 samples, implying significant potential application value in the field of dye wastewater treatment.

3.7 Analysis of the mechanism photocatalytic degradation of RhB

It is known that the catalytic degradation of sewage by TiO_2 under light exposure generates various active free radicals; the most common are superoxide anion radicals ($\cdot O_2^-$), hydroxyl radicals ($\cdot OH$), and holes (h^+).[44] Moreover, the photocatalytic reaction utilizes these highly active free radicals to react with organic pollutant molecules through electron transfer, substitution, and addition. The organic macromolecules degrade into small molecules or inorganic substances.[45] Therefore, in this study, an electron paramagnetic resonance spectrometer (EPR) was used to detect the free radicals produced during the reaction process of sample CPK-TiO_2-10, with DMPO as $\cdot OH$ and $\cdot O_2^-$ capturing agent and TEMO to verify h^+. Fig. 12a and b illustrate that under dark conditions, the CPK-TiO_2-10 sample lacks the characteristic peaks of $\cdot O_2^-$ and $\cdot OH$. However, after irradiating the reaction system in the methanol phase for ten minutes with a mercury lamp UV light, six peak signals become apparent in the EPR spectra shown in Fig. 12a. These signals correspond to the typical signal peaks of DMPO-$\cdot O_2^-$.[46] This observation indicates that $\cdot O_2^-$ is not produced in a dark environment but can be produced when exposed to light. Following a ten-minute irradiation of the reaction system in the aqueous phase with UV light from a mercury lamp, a four-peak signal with a peak intensity ratio of 1 : 2 : 2 : 1 becomes visible in the EPR spectra shown in Fig. 12b. This pattern is a typical signal peak of DMPO-$\cdot OH$.[47] It indicates that $\cdot OH$ is not produced in a dark environment but can be produced when exposed to light. Fig. 12c shows the signal peak of TEMPO, and the signal intensity of TEMPO at 10 minutes of illumination is weaker than that in the dark. It indicates that h^+ can be produced when exposed to light, and can react with TEMPO, therefore, the signal intensity of the TEMPO is weakened.[48,49] EPR tests confirm the production of $\cdot O_2^-$, $\cdot OH$, and h^+ radicals in the CPK-TiO_2-10 photocatalytic degradation system for RhB.

For a more in-depth exploration of the contribution of each active free radical in the CPK-TiO_2-10 photocatalytic system and to identify the predominant active species, free radical trapping experiments were conducted. Upon introducing the capture agent, the degradation efficiency of the dye solution diminished, suggesting that the captured free radical exerts a significant influence on the reaction system. In this experiment, excess *p*-benzoquinone (p-BQ), isopropyl alcohol (IPA), and ethylenediaminetetraacetic acid disodium salt (EDTA-2Na) served as capture agents for $\cdot O_2^-$, $\cdot OH$, and h^+ respectively.[50] Each capture agent effectively scavenged the corresponding radicals without affecting the others. The effects of the corresponding radicals were analyzed by examining the changes in the degradation rate of RhB following the addition of the capture agent. Each of the following solutions—5 mL of 0.25 mol L^{-1} p-BQ, IPA, and EDTA-2Na—was added, respectively. Following a 30 minutes dark adsorption phase, the reaction system underwent a 60 minutes irradiation with a 300 W mercury lamp, and absorbance measurements were taken at ten-minute intervals. The results are depicted in Fig. 12d.

Fig. 12d illustrates that the addition of various capture agents led to varying degrees of inhibition in the degradation of RhB. RhB degradation approached approximately 100% in the comparison solution without the addition of a capture agent.

Open Access Article. Published on 14 May 2024. Downloaded on 1/20/2026 11:48:06 AM.
This article is licensed under a Creative Commons Attribution-NonCommercial 3.0 Unported Licence.

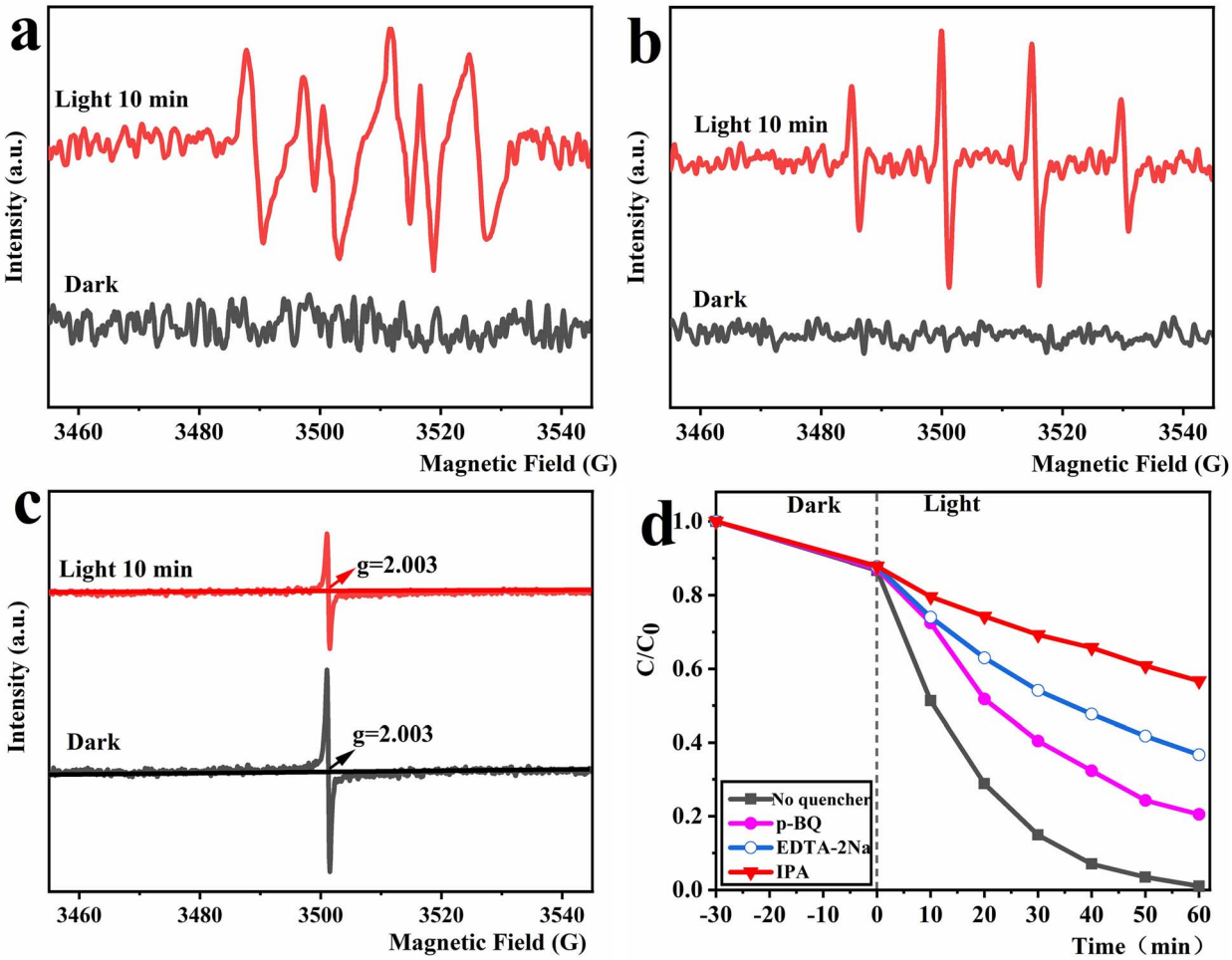

Fig. 12 Electron paramagnetic resonance (EPR) spectra and the results of radical capture experiments: (a) DMPO-$^{\bullet}O_2^-$; (b) DMPO-$^{\bullet}OH$; (c) TEMPO-h^+; and (d) the results from radical trapping experiments.

Upon introducing IPA to capture the $^{\bullet}OH$, the degradation rate of RhB decreased from 100% to 42.43%, representing a decrease of around 58%. This substantial reduction suggests a marked inhibition of the photocatalytic activity of CPK-TiO_2-10. Similarly, the addition of EDTA-2Na to capture the h^+ led to a reduction in the degradation rate of RhB from 100% to 63.31%, marking a reduction of approximately 36%. This indicates a notable inhibition of the photocatalytic activity of CPK-TiO_2-10. The introduction of p-BQ to capture the $^{\bullet}O_2^-$ led to a reduction in the degradation rate of RhB from 100% to 79.53%, representing a reduction of approximately 20%. This suggests an inhibition of the photocatalytic activity of CPK-TiO_2-10, albeit with a more limited effect. Results here also indicate the involvement of $^{\bullet}OH$, h^+, and $^{\bullet}O_2^-$ in the photocatalytic degradation of RhB by CPK-TiO_2-10. These three active free radicals exhibited their effects in the following order: $^{\bullet}OH > h^+ > {}^{\bullet}O_2^-$.

The EPR spectra and the outcomes of the free radical capture test were utilized to deduce the mechanism of the photocatalytic degradation of RhB dye wastewater by CPK-TiO_2 under UV irradiation from a mercury lamp, as illustrated in Scheme 2. Under light irradiation, CPK-TiO_2 absorbs light energy. When the light energy $E \geq E_g$ (band gap energy, Fig. 9b), electrons in the valence band are excited to jump to the conduction band. Simultaneously, the corresponding h^+ is generated in the valence band.[51] Moreover, some electrons and h^+ migrate to the surface of CPK-TiO_2, where some h^+ reacts with H_2O adsorbed on the surface to generate $^{\bullet}OH$. Simultaneously, some electrons react with O_2 adsorbed on the surface to generate $^{\bullet}O_2^-$. Additionally, some $^{\bullet}O_2^-$ undergo further conversion to $^{\bullet}OH$. The free radical capture test outcomes indicated that $^{\bullet}OH$ was the primary active free radical in the photocatalytic degradation of the RhB solution by CPK-TiO_2. This radical is primarily the reaction product of h^+ with H_2O and the subsequent conversion of $^{\bullet}O_2^-$. The RhB molecule undergoes oxidation and degradation into colorless small molecules through the combined action of $^{\bullet}OH$, some h^+, and $^{\bullet}O_2^-$. The photocatalytic degradation process can be assessed by the chemical formulas (1)–(6).

$$\text{CPK-TiO}_2 \xrightarrow{h\nu} h^+ + e^- \quad (1)$$

$$e^- + O_2 \rightarrow {}^{\bullet}O_2^- \quad (2)$$

$$h^+ + H_2O \rightarrow H^+ + {}^{\bullet}OH \quad (3)$$

© 2024 The Author(s). Published by the Royal Society of Chemistry

Open Access Article. Published on 14 May 2024. Downloaded on 1/20/2026 11:48:06 AM.
This article is licensed under a Creative Commons Attribution-NonCommercial 3.0 Unported Licence.

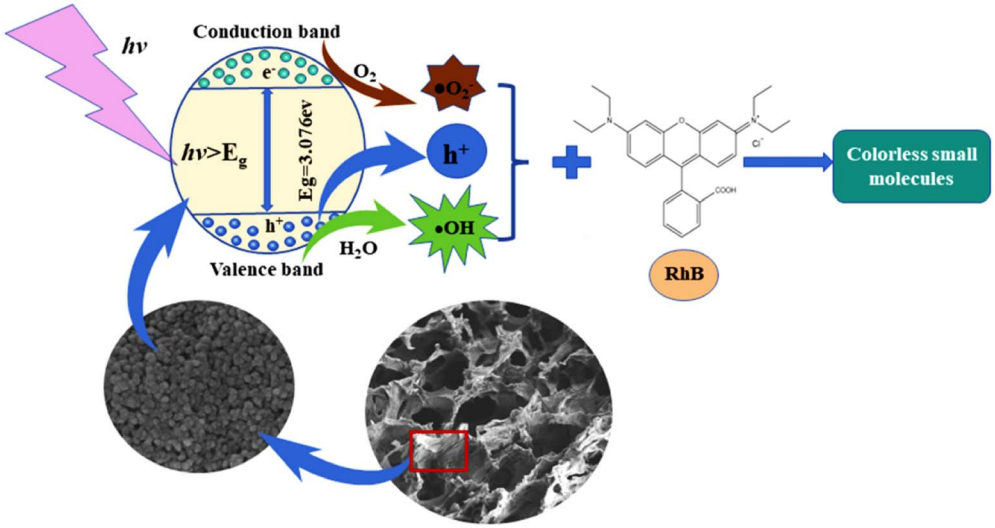

Scheme 2 Schematic diagram of the photocatalytic degradation mechanism of RhB by CPK-TiO_2.

$$O_2 + 2H^+ + e^- \rightarrow H_2O_2 \quad (4)$$

$$H_2O_2 + e^- \rightarrow OH^- + {}^{\bullet}OH \quad (5)$$

$$({}^{\bullet}O_2^- + {}^{\bullet}OH + h^+) + RhB \rightarrow \text{degradation products} \quad (6)$$

4 Conclusion

In this study, based on the design principles of bionics, porous TiO_2 containing C/P/K was synthesized *in situ* from biowaste grapefruit peel and tetrabutyl titanate using a rotary impregnation-calcination two-step method. The raw materials are cost-effective and easily accessible, and the preparation process is straightforward. The complex and delicate hierarchical structure inside the grapefruit peel was utilized to precisely and directionally regulate the nucleation, growth, and structural assembly of TiO_2 nanomaterials. The CPK-TiO_2 exhibits controllable morphology, abundant pores, a large specific surface area, and good crystallinity. Biogenic elements C, P, and K from grapefruit peel self-doping into TiO_2 reduces the rate of photogenerated electron–hole recombination. Additionally, the rotary impregnation technique effectively prevents agglomeration and reduces synthesis time. The degradation performance of RhB simulated dye wastewater is impressive: the degradation rate of RhB reached 100% and the TOC removal rate was 91.34% after 60 minutes of light exposure; a robust degradation effect persists even after five cycles of recycling. Mechanism analysis showed that RhB molecules undergo photodegradation to small molecules under the joint action of $^{\bullet}OH$, h^+, and $^{\bullet}O_2^-$.

In summary, the inorganic functional materials with a porous structure prepared from grapefruit peel as a template exhibit significant potential for application in the photocatalytic degradation of dye wastewater. This research provides design ideas and data support for the preparation of inorganic functional materials.

Author contributions

Ruixiang Wu: investigation, conceptualization, methodology, data curation, formal analysis, writing – original draft. Wenhua Liu: conceptualization, writing – review and editing, supervision, resources, funding acquisition, project administration. Renao Bai: investigation, formal analysis. Xiufang Tian: investigation, formal analysis Weikai, Lin: investigation, software. Lejian, Li: investigation, software. Qianqwei, Ke: investigation.

Conflicts of interest

There are no conflicts to declare.

Acknowledgements

We are grateful for the financial support from the Special Fund Project for Science and Technology Innovation Strategy of Guangdong Province (No. pdjh2021b0916) and the financial support from the 2023 Guangdong Provincial Special Program for Science and Technology Innovation Strategy, supporting city and county technological innovation (major projects + task list) (No. 2023-56).

References

1 S. L. Wear, V. Acuña, R. McDonald and C. Font, *Biol. Conserv.*, 2021, **255**, 109010.
2 J. M. Bidu, B. van der Bruggen, M. J. Rwiza and K. N. Njau, *Water Sci. Technol.*, 2021, **83**, 2363–2376.
3 H. Chen, X. Yu, X. N. Wang, Y. L. He, C. J. Zhang, G. Xue, Z. H. Liu, H. B. Lao, H. L. Song, W. Chen, Y. J. Qian and A. Zhang, *J. Clean. Prod.*, 2021, **326**, 12953.
4 L. M. Bai, S. Wang, Z. Y. Wang, E. L. Hong, Y. Wang, C. H. Xia and B. Q. Wang, *Environ. Pollut.*, 2019, **248**, 516–525.

© 2024 The Author(s). Published by the Royal Society of Chemistry

Open Access Article. Published on 14 May 2024. Downloaded on 1/20/2026 11:48:06 AM. This article is licensed under a Creative Commons Attribution-NonCommercial 3.0 Unported Licence.

5 E. Alinezhada, M. Haghighib, F. Rahmanic, H. Keshizadeha, M. Abdia and K. Naddafia, *J. Environ. Manage.*, 2019, **241**, 32–43.
6 Y. Boyjoo, H. Q. Sun, J. Liu, V. K. Pareek and S. B. Wang, *Chem. Eng. J.*, 2017, **310**, 537–559.
7 T. S. Rajaraman, V. G. Gandhi, V. H. Nguyen and S. P. Parikh, *Appl. Nanosci.*, 2022, **13**, 3925–3944.
8 V. Verma, M. Al-Dossari, J. Singh, M. Rawat, M. G. M. Kordy and M. Shaban, *Polymers*, 2022, **14**, 1444.
9 S. O. Dan and S. H. Khan, *Int. J. Life Sci. Pharma Res.*, 2022, **12**, 215–P233.
10 P. S. Jassal, D. Kaur, R. Prasad and J. Singh, *J. Agric. Food Res.*, 2022, **10**, 100361.
11 X. Y. Wang, S. NLi, P. Chen, F. X. Li, X. M. Hu and T. Hua, *Mater. Today Chem.*, 2022, **23**, 100650.
12 L. X. Zhang, C. H. Ni, H. F. Jiu, H. Chen and G. S. Qi, *J. Mater. Sci.: Mater. Electron.*, 2017, **28**, 6601–6606.
13 A. Sirivallop, T. Areerob and S. Chiarakorn, *Catalysts*, 2020, **10**, 251.
14 A. Sett, M. Gadewar, P. Sharma, M. Deka and U. Bora, *Adv. Nat. Sci.: Nanosci. Nanotechnol.*, 2016, **7**, 025005.
15 A. Girigoswami, B. Deepika, A. K. Pandurangan and K. Girigoswami, *Artif. Cells Nanomed. Biotechnol.*, 2024, **52**(1), 59–68.
16 X. F. Li, T. X. Fan, H. Zhou, S. W. Chow, W. Zhang, D. Zhang, Q. Guo and H. Ogawa, *Adv. Funct. Mater.*, 2009, **19**, 45–56.
17 A. Chen, J. C. Qian, Y. Chen, X. W. Lu, F. Wang and Z. F. Tang, *Powder Technol.*, 2013, **249**, 71–76.
18 N. Turkten, B. Karatas, Y. Karatas, Z. Cinar and M. Bekbolet, *Environ. Prog. Sustain. Energy*, 2022, e14054.
19 C. Zhang, P. Xiao, F. Ni, L. K. Yan, Q. Q. Liu, D. Zhang, J. C. Gu, W. Q. Wang and T. Chen, *ACS Sustainable Chem. Eng.*, 2020, **8**, 5328–5337.
20 J. Z. Han, Y. J. Ping, J. J. Li, Z. Liu, B. Y. Xiong, P. F. Fang and C. Q. He, *Diamond Relat. Mater.*, 2019, **96**, 176–181.
21 W. B. Chai, X. Y. Liu, J. C. Zou, X. Y. Zhang, B. B. Li and T. T. Yin, *Carbohydr. Polym.*, 2015, **132**, 245–251.
22 G. T. Zhu, X. Chen, X. M. He, Z. Zhang, X. S. Li, B. F. Yuan and Y. Q. Feng, *RSC Adv.*, 2015, **5**, 75341–75347.
23 S. J. Zhao, L. Wang, Y. Wang and X. Li, *J. Phys. Chem. Solids*, 2018, **116**, 43–49.
24 Y. Y. Zhang, K. D. Chen, J. C. Zhang, K. Z. Huang, Y. H. Liang, H. W. Hu, X. J. Xu, D. C. Chen, M. L. Chang and Y. Z. Wang, *J. Environ. Chem. Eng.*, 2023, **11**, 109358.
25 Y. Y. Yan, W. C. Kuang, L. J. Shi, X. L. Ye, Y. H. Yang, X. B. Xie, Q. S. Shi and S. Z. Tan, *J. Alloys Compd.*, 2019, **777**, 234–243.
26 G. H. Zhang, T. Y. Zhang, B. Li, S. Jiang, X. Zhang, L. Hai, X. W. Chen, M. Y. Song and P. Du, *Mater. Res. Bull.*, 2017, **94**, 247–256.
27 L. Djerdj and A. M. Tonejc, *J. Alloys Compd.*, 2006, **413**, 159–174.
28 M. C. Biesinger, L. W. M. Lau, A. R. Gerson and R. S. C. Smart, *Appl. Surf. Sci.*, 2010, **257**, 887–898.
29 Y. G. Tan, Z. Shu, J. Zhou, T. T. Li, W. B. Wang and Z. L. Zhao, *Appl. Catal., B*, 2018, **230**, 260–268.
30 P. Qiu, W. Li, K. Kang, B. Park, W. Luo, D. Y. Zhao and J. Khim, *J. Mater. Chem. A*, 2014, **2**, 16452–16458.
31 Y. Zhang, Z. Zhao, J. Chen, L. Cheng, J. Chang, W. Sheng, C. Hu and S. Cao, *Appl. Catal., B*, 2015, **165**, 715–722.
32 J. S. Yuan, Y. Zhang, X. Y. Zhang, J. J. Zhang and S. G. Zhang, *Int. J. Miner., Metall. Mater.*, 2024, **1**(31), 165.
33 X. Li, X. Q. Wang, L. Yuan, L. L. Wang, Y. X. Ma, Y. Wu, Y. B. Xie, R. Cao, Y. R. Xiong and P. Ning, *Chem. Eng. J.*, 2023, **471**, 144573.
34 D. L. Jiang, T. Y. Wang, Q. Xu, D. Li, S. C. Meng and M. Chen, *Appl. Catal., B*, 2017, **201**, 617–628.
35 J. Xiao, Z. C. Pan, B. Zhang, G. Liu, H. C. Zhang, X. F. Song, G. H. Hu, C. M. Xiao, Z. G. Wei and Y. Y. Zheng, *Mater. Lett.*, 2017, **188**, 66–68.
36 W. B. Chai, X. Y. Liu, J. C. Zou, X. Y. Zhang, B. B. Li and T. T. Yin, *Carbohydr. Polym.*, 2015, **132**, 245–251.
37 P. Tasaso, *J. Clean Energy Technol.*, 2014, **2**, 154–157.
38 G. H. Zhang, T. Y. Zhang, B. Li, X. Zhang and X. W. Chen, *J. Alloys Compd.*, 2016, **668**, 113–120.
39 A. C. Martins, A. L. Cazetta, O. Pezoti, J. R. B. Souza, T. Zhang, E. J. Pilau, T. Asefa and V. C. Almeida, *Ceram. Int.*, 2017, **43**, 4411–4418.
40 X. B. Wang, Y. Yan, B. Hao and G. Chen, *Dalton Trans.*, 2014, **43**, 14054–14060.
41 P. Ke, *Preparation of Graphitic Carbon Nitride[1]Based Photocatalysts and Performance Investigation of Visible Light Degradation of Dyeing Wastewater*, Wuhan University of Science and Technology, 2022.
42 H. B. Kim and D. J. Jang, *CrystEngComm*, 2015, **17**, 3325–3332.
43 W. S. Koe, W. C. Chong, Y. L. Pang, C. H. Koo, M. Ebrahim and A. W. Mohammad, *J. Water Proc. Eng.*, 2020, **33**, 101068.
44 X. D. Tang, Z. R. Wang, W. Huang, Q. W. Jing and N. Liu, *Mater. Res. Bull.*, 2018, **105**, 126–132.
45 M. H. Wu, L. Li, N. Liu, D. J. Wang, Y. C. Xue and L. Tang, *Process Saf. Environ. Prot.*, 2018, **118**, 40–58.
46 J. Yang, J. Dai, C. C. Chen and J. C. Zhao, *J. Photochem. Photobiol., A*, 2009, **1**, 66–77.
47 X. Y. Liu, Q. Zhang, B. W. Yu, R. H. Wu, J. X. Mai, R. J. Wang, L. Y. Chen and S. T. Yang, *Catalysts*, 2016, **6**, 146.
48 N. Verma and R. Ananthakrishnan, *ChemPhotoChem*, 2021, **5**, 545–558.
49 W. Y. Ao, J. S. Qu, H. J. Yu, Y. Liu, C. L. Liu, J. Fu, J. J. Dai, X. T. Bi, Y. X. Yuan and Y. J. Jin, *Environ. Res.*, 2022, **214**, 113837.
50 Y. M. Zhu, D. S. Liu, Y. L. Lai and M. Meng, *J. Nanopart. Res.*, 2014, **16**, 2305–2340.
51 F. Xiao, *J. Mater. Chem.*, 2012, **22**, 819–7830.

© 2024 The Author(s). Published by the Royal Society of Chemistry